Nuclear Spin Effects in Optical Lattice Clocks

Martin M. Boyd, Tanya Zelevinsky, Andrew D. Ludlow, Sebastian
Blatt, Thomas Zanon-Willette, Seth M. Foreman, and Jun Ye
JILA, National Institute of Standards and Technology and University of Colorado,
Department of Physics, University of Colorado, Boulder, CO 80309-0440
(Dated: February 1, 2008)

We present a detailed experimental and theoretical study of the effect of nuclear spin on the performance of optical lattice clocks. With a state-mixing theory including spin-orbit and hyperfine interactions, we describe the origin of the $^1S_0$-$^3P_0$ clock transition and the differential g-factor between the two clock states for alkaline-earth(-like) atoms, using ^{87}Sr as an example. Clock frequency shifts due to magnetic and optical fields are discussed with an emphasis on those relating to nuclear structure. An experimental determination of the differential g-factor in ^{87}Sr is performed and is in good agreement with theory. The magnitude of the tensor light shift on the clock states is also explored experimentally. State specific measurements with controlled nuclear spin polarization are discussed as a method to reduce the nuclear spin-related systematic effects to below 10^{-17} in lattice clocks.

Optical clocks [1] based on alkaline-earth atoms confined in an optical lattice [2] are being intensively explored as a route to improve state of the art clock accuracy and precision. Pursuit of such clocks is motivated mainly by the benefits of Lamb-Dicke confinement which allows high spectral resolution [3, 4], and high accuracy [5, 6, 7, 8] with the suppression of motional effects, while the impact of the lattice potential can be eliminated using the Stark cancelation technique [9, 10, 11, 12]. Lattice clocks have the potential to reach the impressive accuracy level of trapped ion systems, such as the Hg$^+$ optical clock [13], while having an improved stability due to the large number of atoms involved in the measurement. Most of the work performed thus far for lattice clocks has been focused on the nuclear-spin induced $^1S_0$-$^3P_0$ transition in ^{87}Sr. Recent experimental results are promising for development of lattice clocks as high performance optical frequency standards. These include the confirmation that hyperpolarizability effects will not limit the clock accuracy at the 10^{-17} level [12], observation of transition resonances as narrow as 1.8 Hz [3], and the excellent agreement between high accuracy frequency measurements performed by three independent laboratories [5, 6, 7, 8] with clock systematics associated with the lattice technique now controlled below 10^{-15} [6]. A main effort of the recent accuracy evaluations has been to minimize the effect that nuclear spin ($I = 9/2$ for ^{87}Sr) has on the performance of the clock. Specifically, a linear Zeeman shift is present due to the same hyperfine interaction which provides the clock transition, and magnetic sublevel-dependent light shifts exist, which can complicate the stark cancelation techniques. To reach accuracy levels below 10^{-17}, these effects need to be characterized and controlled.

The long coherence time of the clock states in alkaline earth atoms also makes the lattice clock an intriguing system for quantum information processing. The closed electronic shell should allow independent control of electronic and nuclear angular momenta, as well as protection of the nuclear spin from environmental perturbation,

providing a robust system for coherent manipulation[14]. Recently, protocols have been presented for entangling nuclear spins in these systems using cold collisions [15] and performing coherent nuclear spin operations while cooling the system via the electronic transition [16].

Precise characterization of the effects of electronic and nuclear angular-momentum-interactions and the resultant state mixing is essential to lattice clocks and potential quantum information experiments, and therefore is the central focus of this work. The organization of this paper is as follows. First, state mixing is discussed in terms of the origin of the clock transition as well as a basis for evaluating external field sensitivities on the clock transition. In the next two sections, nuclear-spin related shifts of the clock states due to both magnetic fields and the lattice trapping potential are discussed. The theoretical development is presented for a general alkaline-earth type structure, using ^{87}Sr only as an example (Fig. 1), so that the results can be applied to other species with similar level structure, such as Mg, Ca, Yb, Hg, Zn, Cd, Al$^+$, and In$^+$. Following the theoretical discussion is a detailed experimental investigation of these nuclear spin related effects in ^{87}Sr, and a comparison to the theory sections. Finally, the results are discussed in the context of the performance of optical lattice clocks, including a comparison with recent proposals to induce the clock transition using external fields in order to eliminate nuclear spin effects [17, 18, 19, 20, 21, 22]. The appendix contains additional details on the state mixing and magnetic sensitivity calculations.

I. STATE MIXING IN THE $nsnp$ CONFIGURATION

To describe the two-electron system in intermediate coupling, we follow the method of Breit and Wills [23] and Lurio [24] and write the four real states of the $ns\,np$ configuration as expansions of pure spin-orbit (LS) cou-
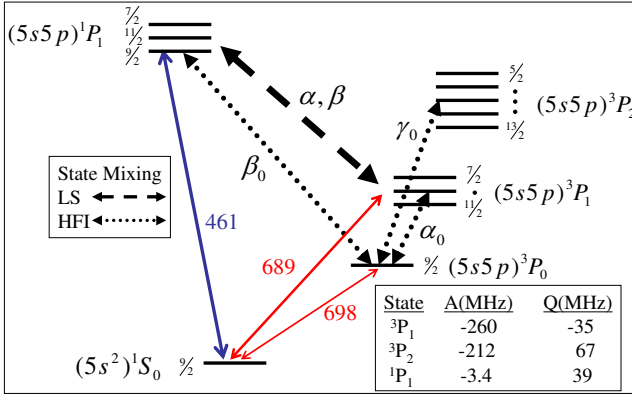
FIG. 1: (color online) Simplified ^{87}Sr energy level diagram (not to scale). Relevant optical transitions discussed in the text are shown as solid arrows, with corresponding wavelengths given in nanometers. Hyperfine structure sublevels are labeled by total angular momentum F, and the magnetic dipole (A) and electric quadrupole (Q, equivalent to the hyperfine B coefficient) coupling constants are listed in the inset. State mixing of the $^1P_1$ and $^3P_1$ states due to the spin-orbit interaction is shown as a dashed arrow. Dotted arrows represent the hyperfine induced state mixing of the $^3P_0$ state with the other $F = 9/2$ states in the $5s5p$ manifold.

pling states,

$$
\begin{aligned}
|^3P_0\rangle &= |^3P_0^0\rangle \\
|^3P_1\rangle &= \alpha|^3P_1^0\rangle + \beta|^1P_1^0\rangle \\
|^3P_2\rangle &= |^3P_2^0\rangle \\
|^1P_1\rangle &= -\beta|^3P_1^0\rangle + \alpha|^1P_1^0\rangle.
\end{aligned}
\tag{1}
$$

Here the intermediate coupling coefficients α and β (0.9996 and -0.0286 respectively for Sr) represent the strength of the spin-orbit induced state mixing between singlet and triplet levels, and can be determined from experimentally measured lifetimes of $^1P_1$ and $^3P_1$ (see Eq. 15 in the appendix). This mixing process results in a weakly allowed $^1S_0$-$^3P_1$ transition (which would otherwise be spin-forbidden), and has been used for a variety of experiments spanning different fields of atomic physics. In recent years, these intercombination transitions have provided a unique testing ground for studies of narrow-line cooling in Sr [25, 26, 27, 28, 29] and Ca [30, 31], as well as the previously unexplored regime of photoassociation using long lived states [32, 33, 34]. These transitions have also received considerable attention as potential optical frequency standards [35, 36, 37], owing mainly to the high line quality factors and insensitivity to external fields. Fundamental symmetry measurements, relevant to searches of physics beyond the standard model, have also made use of this transition in Hg [38]. Furthermore, the lack of hyperfine structure in the bosonic isotopes ($I = 0$) can simplify comparison between experiment and theory.

The hyperfine interaction (HFI) in fermionic isotopes provides an additional state mixing mechanism between states having the same total spin F, mixing the pure $^3P_0$ state with the $^3P_1$, $^3P_2$ and $^1P_1$ states.

$$
|^3P_0\rangle = |^3P_0^0\rangle + \alpha_0|^3P_1\rangle + \beta_0|^1P_1\rangle + \gamma_0|^3P_2^0\rangle. \tag{2}
$$

The HFI mixing coefficients α_0, β_0, and γ_0 (2×10^{-4}, -4×10^{-6}, and 4×10^{-6} respectively for ^{87}Sr) are defined in Eq. 16 of the appendix and can be related to the hyperfine splitting in the P states, the fine structure splitting in the ^3P states, and the coupling coefficients α and β [23, 24]. The $^3P_0$ state can also be written as a combination of pure states using Eq. 1,

$$
\begin{aligned}
|^3P_0\rangle =& |^3P_0^0\rangle + (\alpha_0\alpha - \beta_0\beta)|^3P_1^0\rangle \\
&+ (\alpha_0\beta + \beta_0\alpha)|^1P_1^0\rangle + \gamma_0|^3P_2^0\rangle.
\end{aligned}
\tag{3}
$$

The HFI mixing enables a non-zero electric-dipole transition via the pure $^1P_1^0$ state, with a lifetime which can be calculated given the spin-orbit and HFI mixing coefficients, the $^3P_1$ lifetime, and the wavelengths (λ) of the $^3P_0$ and $^3P_1$ transitions from the ground state [39].

$$
\tau^{^3P_0} = \left(\frac{\lambda^{^3P_0-^1S_0}}{\lambda^{^3P_1-^1S_0}}\right)^3 \frac{\beta^2}{(\alpha_0\beta + \beta_0\alpha)^2}\tau^{^3P_1}. \tag{4}
$$

In the case of Sr, the result is a natural lifetime on the order of 100 seconds [9, 40, 41], compared to that of a bosonic isotope where the lifetime approaches 1000 years [41]. Although the 100 second coherence time of the excited state exceeds other practical limitations in current experiments, such as laser stability or lattice lifetime, coherence times approaching one second have been achieved [3]. The high spectral resolution has allowed a study of nuclear-spin related effects in the lattice clock system discussed below.

The level structure and state mixing discussed here are summarized in a simplified energy diagram, shown in Fig. 1, which gives the relevant atomic structure and optical transitions for the $5s5p$ configuration in ^{87}Sr.

II. THE EFFECT OF EXTERNAL MAGNETIC FIELDS

With the obvious advantages in spectroscopic precision of the $^1S_0$-$^3P_0$ transition in an optical lattice, the sensitivity of the clock transition to external field shifts is a central issue in developing the lattice clock as an atomic frequency standard. To evaluate the magnetic sensitivity of the clock states, we follow the treatment of Ref. [24] for the intermediate coupling regime described by Eqns. 1-3 in the presence of a weak magnetic field. A more general treatment for the case of intermediate fields is provided in the appendix. The Hamiltonian for the Zeeman interaction in the presence of a weak magnetic field B along the z-axis is given as

$$
H_Z = (g_sS_z + g_lL_z - g_II_z)\mu_0B. \tag{5}
$$

Here $g_s \simeq 2$ and $g_l = 1$ are the spin and orbital angular momentum g-factors, and S_z, L_z, and I_z are the z-components of the electron spin, orbital, and nuclear spin angular momentum respectively. The nuclear g-factor, g_I, is given by $g_I = \frac{\mu_I(1-\sigma_d)}{\mu_0|I|}$, where μ_I is the nuclear magnetic moment, σ_d is the diamagnetic correction and $\mu_0 = \frac{\mu_B}{h}$. Here, μ_B is the Bohr magneton, and h is Planck's constant. For ^{87}Sr, the nuclear magnetic momement and diamagnetic correction are $\mu_I = -1.0924(7)\mu_N$ [42] and $\sigma_d = 0.00345$ [43] respectively, where μ_N is the nuclear magneton. In the absence of state mixing, the $^3P_0$ g-factor would be identical to the $^1S_0$ g-factor (assuming the diamagnetic effect differs by a negligible amount for different electronic states), equal to g_I. However since the HFI modifies the $^3P_0$ wavefunction, a differential g-factor, δg, exists between the two states. This can be interpreted as a paramagnetic shift arising due to the distortion of the electronic orbitals in the triplet state, and hence the magnetic moment [44]. δg is given by

$$
\begin{aligned}
\delta g = & -\frac{\langle {}^3P_0|H_Z|{}^3P_0\rangle - \langle {}^3P_0^0|H_Z|{}^3P_0^0\rangle}{m_F\mu_0 B} \\
= & -2\left(\alpha_0\alpha - \beta_0\beta\right)\frac{\langle {}^3P_0^0, m_F|H_Z|{}^3P_1^0, F=I, m_F\rangle}{m_F\mu_0 B} \\
& + \mathcal{O}(\alpha_0^2, \beta_0^2, \gamma_0^2, \ldots).
\end{aligned} \tag{6}
$$

Using the matrix element given in the appendix for ^{87}Sr $(I = 9/2)$, we find $\langle {}^3P_0^0, m_F|H_Z|{}^3P_1^0, F = \frac{9}{2}, m_F\rangle = \frac{2}{3}\sqrt{\frac{2}{33}}m_F\mu_0 B$, corresponding to a modification of the $^3P_0$ g-factor by $\sim 60\%$. Note that the sign in Eq. 6 differs from that reported in [39, 44] due to our choice of sign for the nuclear term in the Zeeman Hamiltonian (opposite of that found in Ref. [24]). The resulting linear Zeeman shift $\Delta_B^{(1)} = -\delta g m_F\mu_0 B$ of the $^1S_0$-$^3P_0$ transition is on the order of $\sim 110 \times m_F$ Hz/G (1 G = 10^{-4} Tesla). This is an important effect for the development of lattice clocks, as stray magnetic fields can broaden the clock transition (deteriorate the stability) if multiple sublevels are used. Furthermore, imbalanced population among the sublevels or mixed probe polarizations can cause frequency errors due to line shape asymmetries or shifts. It has been demonstrated that if a narrow resonance is achieved (10 Hz in the case of Ref. [6]), these systematics can be controlled at 5×10^{-16} for stray fields of less than 5 mG. To reduce this effect, one could employ narrower resonances or magnetic shielding.

An alternative measurement scheme is to measure the average transition frequency between m_F and $-m_F$ states of to cancel the frequency shifts. This requires application of a bias field to resolve the sublevels, and therefore the second order Zeeman shift $\Delta_B^{(2)}$ must be considered. The two clock states are both $J = 0$ so the shift $\Delta_B^{(2)}$ arises from levels separated in energy by the fine-structure splitting, as opposed to the more traditional case of alkali(-like) atoms where the second order shift arises from nearby hyperfine levels. The shift of the clock transition is dominated by the interaction of
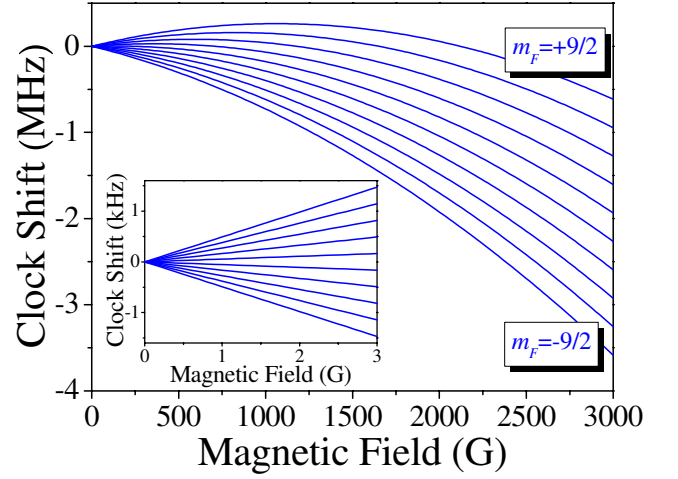

FIG. 2: (color online) A Breit-Rabi diagram for the $^1S_0$-$^3P_0$ clock transition using Eq. 22 with $\delta g\mu_0 = -109$ Hz/G. Inset shows the linear nature of the clock shifts at the fields relevant for the measurement described in the text.

the $^3P_0$ and $^3P_1$ states since the ground state is separated from all other energy levels by optical frequencies. Therefore, the total Zeeman shift of the clock transition Δ_B is given by

$$
\begin{aligned}
\Delta_B &= \Delta_B^{(1)} + \Delta_B^{(2)} \\
&= \Delta_B^{(1)} - \sum_{F'}\frac{|\langle {}^3P_0, F, m_F|H_Z|{}^3P_1, F', m_F\rangle|^2}{\nu_{{}^3P_1, F'} - \nu_{{}^3P_0}}.
\end{aligned} \tag{7}
$$

The frequency difference in the denominator is mainly due to the fine-structure splitting and is nearly independent of F', and can therefore be pulled out of the summation. In terms of the pure states, and ignoring terms of order α_0, β_0, β^2, and smaller, we have

$$
\begin{aligned}
\Delta_B^{(2)} &\simeq -\alpha^2\frac{\sum_{F'}|\langle {}^3P_0^0, F, m_F|H_Z|{}^3P_1^0, F', m_F\rangle|^2}{\nu_{{}^3P_1} - \nu_{{}^3P_0}} \\
&= -\frac{2\alpha^2(g_l - g_s)^2\mu_0^2}{3(\nu_{{}^3P_1} - \nu_{{}^3P_0})}B^2,
\end{aligned} \tag{8}
$$

where we have used the matrix elements given in the appendix for the case $F = 9/2$. From Eq. 8 the second order Zeeman shift (given in Hz for a magnetic field given in Gauss) for ^{87}Sr is $\Delta_B^{(2)} = -0.233B^2$. This is consistent with the results obtained in Ref. [20] and [45] for the bosonic isotope. Inclusion of the hyperfine splitting into the frequency difference in the denominator of Eq. 7 yields an additional term in the second order shift proportional to m_F^2 which is more that 10^{-6} times smaller than the main effect, and therefore negligible. Notably, the fractional frequency shift due to the second order Zeeman effect of 5×10^{-16} G^{-2} is nearly 10^8 times smaller than that of the Cs [46, 47] clock transition, and more than an order of magnitude smaller than that present in Hg$^+$ [13], Sr$^+$ [48, 49], and Yb$^+$ [50, 51] ion optical clocks.

A Breit-Rabi like diagram is shown in Fig. 2, giving the shift of the $^1S_0$-$^3P_0$ transition frequency for different

m_F sublevels (assuming $\Delta m = 0$ for π transitions), as a function of magnetic field. The calculation is performed using an analytical Breit-Rabi formula (Eq. 22) provided in the appendix. The result is indistinguishable from the perturbative derivation in this section, even for fields as large as 10^4 G.

III. THE EFFECT OF THE OPTICAL LATTICE POTENTIAL

In this section we consider the effect of the confining potential on the energy shifts of the nuclear sublevels. In the presence of a lattice potential of depth U_T, formed by a laser linearly polarized along the axis of quantization defined by an external magnetic field B, the level shift of a clock state ($h\Delta_{g/e}$) from its bare energy is given by

$$
\begin{aligned}
\Delta_e = & -m_F(g_I + \delta g)\mu_0 B - \kappa_e^S \frac{U_T}{E_R} - \kappa_e^V \xi m_F \frac{U_T}{E_R} \\
& - \kappa_e^T \left(3m_F^2 - F(F+1)\right) \frac{U_T}{E_R} \\
\Delta_g = & -m_F g_I \mu_0 B - \kappa_g^S \frac{U_T}{E_R} - \kappa_g^V \xi m_F \frac{U_T}{E_R} \\
& - \kappa_g^T \left(3m_F^2 - F(F+1)\right) \frac{U_T}{E_R}.
\end{aligned} \tag{9}
$$

Here, κ^S, κ^V, and κ^T are shift coefficients proportional to the scalar, vector (or axial), and tensor polarizabilities, and subscripts e and g refer to the excited ($^3P_0$) and ground ($^1S_0$) states respectively. E_R is the energy of a lattice photon recoil and U_T/E_R characterizes the lattice intensity. The vector ($\propto m_F$) and tensor ($\propto m_F^2$) light shift terms arise solely from the nuclear structure and depend on the orientation of the light polarization and the bias magnetic field. The tensor shift coefficient includes a geometric scaling factor which varies with the relative angle ϕ of the laser polarization axis and the axis of quantization, as $3\cos^2\phi - 1$. The vector shift, which can be described as an pseudo-magnetic field along the propagation axis of the trapping laser, depends on the trapping geometry in two ways. First, the size of the effect is scaled by the degree of elliptical polarization ξ, where $\xi = 0$ ($\xi = \pm 1$) represents perfect linear (circular) polarization. Second, for the situation described here, the effect of the vector light shift is expected to be orders of magnitude smaller than the Zeeman effect, justifying the use of the bias magnetic field direction as the quantization axis for all of the m_F terms in Eq. 9. Hence the shift coefficient depends on the relative angle between the pseudo-magnetic and the bias magnetic fields, vanishing in the case of orthogonal orientation [52]. A more general description of the tensor and vector effects in alkaline-earth systems for the case of arbitrary elliptical polarization can be found in Ref. [10]. Calculations of the scalar, vector, and tensor shift coefficients have been performed elsewhere for Sr, Yb, and Hg [9, 10, 11, 52] and will not be discussed here. Hyperpolarizability effects ($\propto U_T^2$) [9, 10, 11, 12] are ignored in Eq. 9 as they

are negligible in ^{87}Sr at the level of 10^{-17} for the range of lattice intensities used in current experiments [12]. The second order Zeeman term has been omitted but is also present.

Using Eq. 9 we can write the frequency of a π-transition ($\Delta m_F = 0$) from a ground state m_F as

$$
\begin{aligned}
\nu_{\pi_{m_F}} = & \nu_c - \left(\Delta\kappa^S - \Delta\kappa^T F(F+1)\right) \frac{U_T}{E_R} \\
& - \left(\Delta\kappa^V m_F \xi + \Delta\kappa^T 3m_F^2\right) \frac{U_T}{E_R} \\
& - \delta g m_F \mu_0 B,
\end{aligned} \tag{10}
$$

where the shift coefficients due to the differential polarizabilities are represented as $\Delta\kappa$, and ν_c is the bare clock frequency. The basic principle of the lattice clock technique is to tune the lattice wavelength (and hence the polarizabilities) such that the intensity-dependent frequency shift terms are reduced to zero. Due to the m_F-dependence of the third term of Eq. 10, the Stark shifts cannot be completely compensated for all of the sublevels simultaneously. Or equivalently, the magic wavelength will be different depending on the sublevel used. The significance of this effect depends on the magnitude of the tensor and vector terms. Fortunately, in the case of the $^1S_0$-$^3P_0$ transition the clock states are nearly scalar, and hence these effects are expected to be quite small. While theoretical estimates for the polarizabilities have been made, experimental measurements are unavailable for the vector and tensor terms. The frequencies of $\sigma^\pm$ ($\Delta m_F = \pm 1$) transitions from a ground m_F state are similar to the π-transitions, given by

$$
\begin{aligned}
\nu_{\sigma_{m_F}^\pm} = & \nu_c - \left(\Delta\kappa^S - \Delta\kappa^T F(F+1)\right) \frac{U_T}{E_R} \\
& - \left((\kappa_e^V(m_F \pm 1) - \kappa_g^V m_F)\xi\right) \frac{U_T}{E_R} \\
& - \left(\kappa_e^T 3(m_F \pm 1)^2 - \kappa_g^T 3m_F^2\right) \frac{U_T}{E_R} \\
& - (\pm g_I + \delta g(m_F \pm 1))\mu_0 B.
\end{aligned} \tag{11}
$$

IV. EXPERIMENTAL DETERMINATION OF FIELD SENSITIVITIES

To explore the magnitude of the various m_F-dependent shifts in Eq. 10, a differential measurement scheme can be used to eliminate the large shifts common to all levels. Using resolved sublevels one can extract m_F sensitivities by measuring the splitting of neighboring states. This is the approach taken here. A diagram of our spectroscopic setup is shown in Fig. 3(a). ^{87}Sr atoms are captured from a thermal beam into a magneto-optical trap (MOT), based on the $^1S_0$-$^1P_1$ cycling transition. The atoms are then transferred to a second stage MOT for narrow line cooling using a dual frequency technique [26]. Full details of the cooling and trapping system used in this work are discussed elsewhere [5, 28]. During the cooling process, a vertical one-dimensional lattice is overlapped
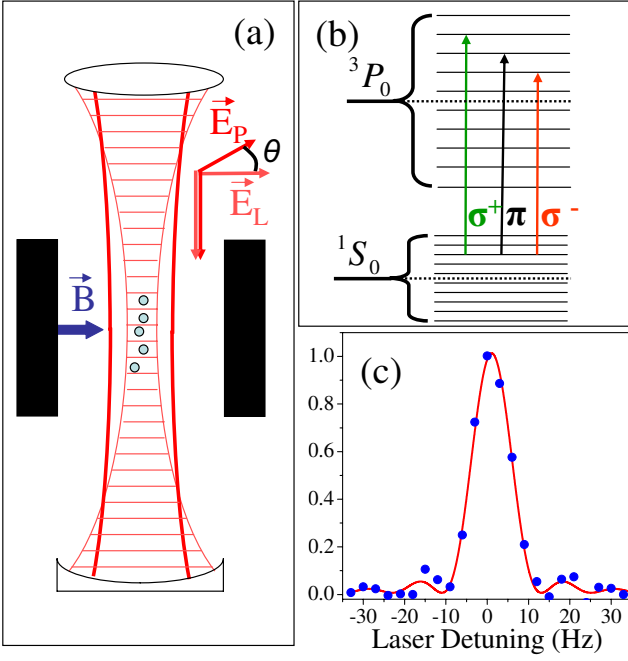
FIG. 3: (color online) (a) Schematic of the experimental apparatus used here. Atoms are confined in a nearly vertical optical lattice formed by a retro-reflected 813 nm laser. A 698 nm probe laser is co-aligned with the lattice. The probe polarization E_P can be varied by an angle θ relative to that of the linear lattice polarization E_L. A pair of Helmholtz coils (blue) is used to apply a magnetic field along the lattice polarization axis. (b) Nuclear structure of the $^1S_0$ and $^3P_0$ clock states. The large nuclear spin ($I = 9/2$) results in 28 total transitions, and the labels π, σ^+, and σ^- represent transitions where m_F changes by 0, +1, and −1 respectively. (c) Observation of the clock transition without a bias magnetic field. The $^3P_0$ population (in arbitrary units) is plotted (blue dots) versus the probe laser frequency for $\theta = 0$, and a fit to a sinc-squared lineshape yields a Fourier-limited linewidth of 10.7(3) Hz. Linewidths as narrow as 5 Hz have been observed under similar conditions and when the probe time is extended to 500 ms.

with the atom cloud. We typically load $\sim 10^4$ atoms into the lattice at a temperature of $\sim 1.5\mu$K. The lattice is operated at the Stark cancelation wavelength [6, 12] of 813.4280(5) nm with a trap depth of $U_0 = 35E_R$. A Helmholtz coil pair provides a field along the lattice polarization axis for resolved sub-level spectroscopy. Two other coil pairs are used along the other axes to zero the orthogonal fields. The spectroscopy sequence for the $^1S_0$-$^3P_0$ clock transition begins with an 80 ms Rabi pulse from a highly stabilized diode laser [53] that is co-propagated with the lattice laser. The polarization of the probe laser is linear at an angle θ relative to that of the lattice. A shelved detection scheme is used, where the ground state population is measured using the $^1S_0$-$^1P_1$ transition. The $^3P_0$ population is then measured by pumping the atoms through intermediate states using $^3P_0$-$^3S_1$, $^3P_2$-$^3S_1$, and the natural decay of $^3P_1$, before applying a second $^1S_0$-
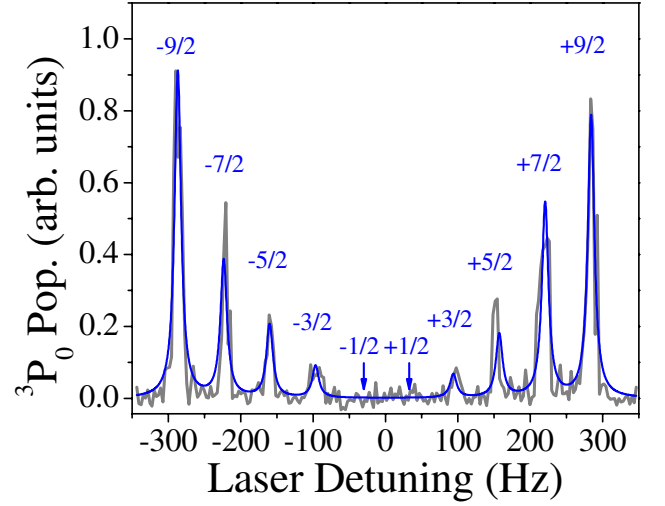

FIG. 4: (color online) Observation of the $^1S_0$-$^3P_0$ π-transitions ($\theta = 0$) in the presence of a 0.58 G magnetic field. Data is shown in grey and a fit to the eight observable lineshapes is shown as a blue curve. The peaks are labeled by the ground state m_F-sublevel of the transition. The relative transition amplitudes for the different sublevels are strongly influenced by the Clebsch-Gordan coefficients. Here, transition linewidths of 10 Hz are used. Spectra as narrow as 1.8 Hz can be achieved under similar conditions if the probe time is extended to 500 ms.

$^1P_1$ pulse. The 461 nm pulse is destructive, so for each frequency step of the probe laser the $\sim$800 ms loading and cooling cycle is repeated.

When π polarization is used for spectroscopy ($\theta = 0$), the large nuclear spin provides ten possible transitions, as shown schematically in Fig. 3(b). Figure 3(c) shows a spectroscopic measurement of these states in the absence of a bias magnetic field. The suppression of motional effects provided by the lattice confinement allows observation of extremely narrow lines [3, 4, 19], in this case having Fourier-limited full width at half maximum (FWHM) of $\sim$10 Hz (quality factor of 4×10^{13}). In our current apparatus the linewidth limitation is 5 Hz with degenerate sublevels and 1.8 Hz when the degeneracy is removed [3]. The high spectral resolution allows for the study of nuclear spin effects at small bias fields, as the ten sublevels can easily be resolved with a few hundred mG. An example of this is shown in Fig. 4, where the ten transitions are observed in the presence of a 0.58 G bias field. This is important for achieving a high accuracy measurement of δg as the contribution from magnetic-field-induced state mixing is negligible. To extract the desired shift coefficients we note that for the π transitions we have a frequency gap between neighboring lines of

$$f_{\pi,m_F} = \nu_{\pi_{m_F}} - \nu_{\pi_{m_F-1}}$$
$$= -\delta g \mu_0 B - \Delta\kappa^V \xi \frac{U_T}{E_R} - \Delta\kappa^T 3(2m_F - 1)\frac{U_T}{E_R}. \quad (12)$$
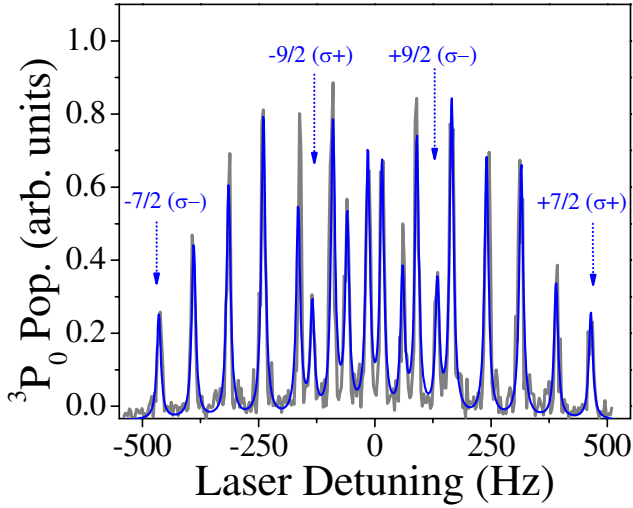
From Eq. 12, we see that by measuring the differences in

FIG. 5: (color online) Observation of the 18 σ transitions when the probe laser polarization is orthogonal to that of the lattice ($\theta = \frac{\pi}{2}$). Here, a field of 0.69 G is used. The spectroscopic data is shown in grey and a fit to the data is shown as a blue curve. Peak labels give the ground state sublevel of the transition, as well as the excitation polarization.
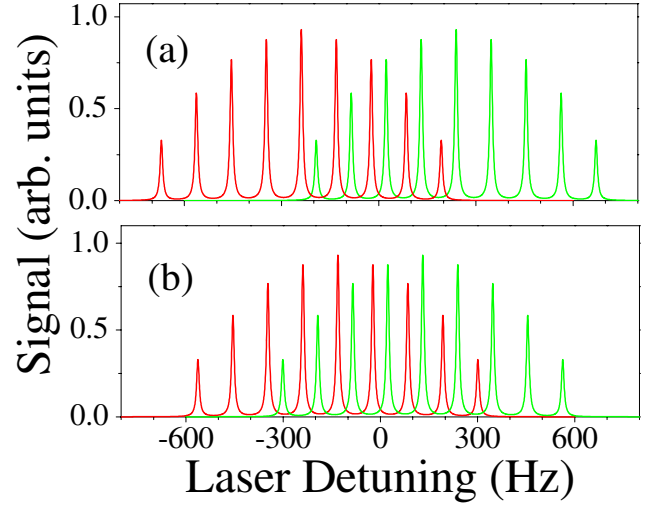

FIG. 6: (color online) Calculation of the 18 σ transition frequencies in the presence of a 1 G bias field, including the influence of Clebsch-Gordan coefficients. The green (red) curves show the σ^+ (σ^-) transitions. (a) Spectral pattern for g-factors $g_I \mu_0 = -185$ Hz/G and $\delta g \mu_0 = -109$ Hz/G. (b) Same pattern as in (a) but with $\delta g \mu_0 = +109$ Hz/G. The qualitative difference in the relative positions of the transitions allows determination of the sign of δg compared to that of g_I.

frequency of two spectroscopic features, the three terms of interest (δg, $\Delta \kappa^V$, and $\Delta \kappa^T$) can be determined independently. The differential g factor can be determined by varying the magnetic field. The contribution of the last two terms can be extracted by varying the intensity of the standing wave trap, and can be independently determined since only the tensor shift depends on m_F.

While the π transitions allow a simple determination of δg, the measurement requires a careful calibration of the magnetic field and a precise control of the probe laser frequency over the ~ 500 seconds required to produce a scan such as in Fig. 4. Any linear laser drift will appear in the form of a smaller or larger δg, depending on the laser scan direction. Furthermore, the measurement can not be used to determine the sign of δg as an opposite sign would yield an identical spectral pattern. In an alternative measurement scheme, we instead polarize the probe laser perpendicular to the lattice polarization ($\theta = \frac{\pi}{2}$) to excite both σ^+ and σ^- transitions. In this configuration, 18 spectral features are observed and easily identified (Fig. 5). Ignoring small shifts due to the lattice potential, δg is given by extracting the frequency splitting between adjacent transitions of a given polarization (all σ^+ or all σ^- transitions) as $f_{\sigma^\pm, m_F} = \nu_{\sigma^\pm_{m_F}} - \nu_{\sigma^\pm_{m_F-1}} = -\delta g \mu_0 B$. If we also measure the frequency difference between σ^+ and σ^- transitions from the same sublevel, $f_{d,m_F} = \nu_{\sigma^+_{m_F}} - \nu_{\sigma^-_{m_F}} = -2(g_I + \delta g)\mu_0 B$, we find that the differential g-factor can be determined from the ratio of these frequencies as

$$\delta g = \frac{g_I}{\frac{f_{d,m_F}}{2f_{\sigma^\pm, m_F}} - 1}. \tag{13}$$

In this case, prior knowledge of the magnetic field is not required for the evaluation, nor is a series of measurement at different fields, as δg is instead directly determined from the line splitting and the known $^1S_0$ g factor g_I. The field calibration and the δg measurement are in fact done simultaneously, making the method immune to some systematics which could mimic a false field, such as linear laser drift during a spectroscopic scan or slow magnetic field variations. Using the σ transitions also eliminates the sign ambiguity which persists when using the π transitions for measuring δg. While we can not extract the absolute sign, the recovered spectrum is sensitive to the relative sign between g_I and δg. This is shown explicitly in Fig. 6 where the positions of the transitions have been calculated in the presence of a ~ 1 G magnetic field. Figure 6(a) shows the spectrum when the signs of g_I and δg are the same while in Fig. 6(b) the signs are opposite. The two plots show a qualitative difference between the two possible cases. Comparing Fig. 5 and Fig. 6 it is obvious that the hyperfine interaction *increases* the magnitude of the $^3P_0$ g-factor (δg has the same sign as g_I). We state this point explicitly because of recent inconsistencies in theoretical estimates of the relative sign of δg and g_I in the ^{87}Sr literature [7, 8].

To extract the magnitude of δg, data such as in Fig. 5 are fit with eighteen Lorentzian lines, and the relevant splitting frequencies f_{d,m_F} and $f_{\sigma^\pm}$ are extracted. Due to the large number of spectral features, each experimental spectrum yields 16 measurements of δg. A total of 31 full spectra was taken, resulting in an average value of $\delta g \mu_0 = -108.4(4)$ Hz/G where the uncertainty is the
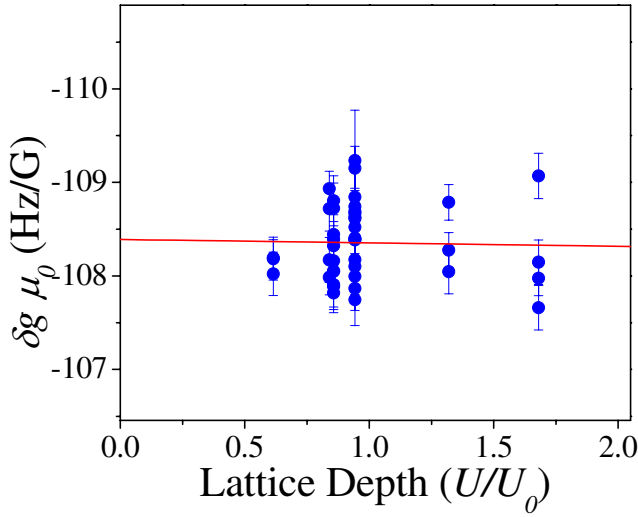
FIG. 7: (color online) Summary of δg-measurements for different lattice intensities. Each data point (and uncertainty) represents the δg value extracted from a full $\sigma^\pm$ spectrum such as in Fig. 5. Linear extrapolation (red line) to zero lattice intensity yields a value $-108.4(1)$ Hz/G.
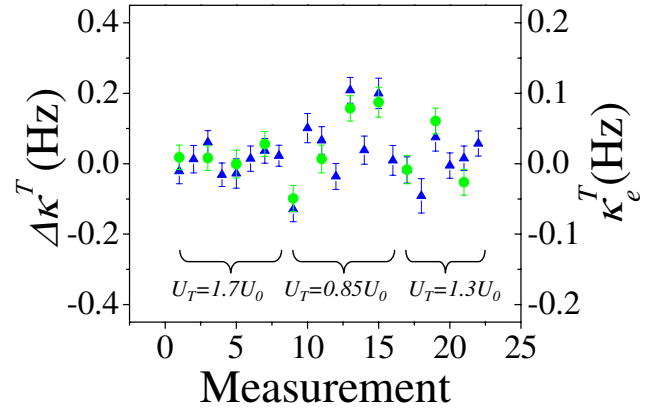

FIG. 8: (color online) Measurement of the tensor shift coefficients $\Delta\kappa^T$ (blue triangles), and κ_e^T (green circles), using σ spectra and Eq. 14. The measured coefficients show no statistically significant trap depth dependence while varying the depth from 0.85–1.7 U_0.

standard deviation of the measured value. To check for sources of systematic error, the magnetic field was varied to confirm the field independence of the measurement. We also varied the clock laser intensity by an order of magnitude to check for Stark and line pulling effects. It is also necessary to consider potential measurement errors due to the optical lattice since in general the splitting frequencies f_{d,m_F} and $f_{\sigma^\pm}$ will depend on the vector and tensor light shifts. For fixed fields, the vector shift is indistinguishable from the linear Zeeman shift (see Eqs. 10-12) and can lead to errors in calibrating the field for a δg measurement. In this work, a high quality linear polarizer (10^{-4}) is used which would in principle eliminate the vector shift. The nearly orthogonal orientation should further reduce the shift. However, any birefringence of the vacuum windows or misalignment between the lattice polarization axis and the magnetic field axis can lead to a non-zero value of the vector shift. To measure this effect in our system, we varied the trapping depth over a range of $\sim (0.6 - 1.7)U_0$ and extrapolated δg to zero intensity, as shown in Fig. 7. Note that this measurement also checks for possible errors due to scalar and tensor polarizabilites as their effects also scale linearly with the trap intensity. We found that the δg-measurement was affected by the lattice potential by less then 0.1%, well below the uncertainty quoted above.

Unlike the vector shift, the tensor contribution to the sublevel splitting is distinguishable from the magnetic contribution even for fixed fields. Adjacent σ transitions can be used to measure $\Delta\kappa^T$ and κ_e^T due to the m_F^2 dependence of the tensor shift. An appropriate choice of transition comparisons results in a measurement of the tensor shift without any contributions from magnetic or vector terms. To enhance the sensitivity of our measure-

ment we focus mainly on the transitions originating from states with large m_F; for example, we find that

$$
\begin{aligned}
\Delta\kappa^T &= -\frac{f_{\sigma^+,m_F=7/2} - f_{\sigma^+,m_F=-7/2}}{42\frac{U_T}{E_R}} \\
\kappa_e^T &= -\frac{f_{d,m_F=7/2} - f_{d,m_F=-7/2}}{84\frac{U_T}{E_R}},
\end{aligned}
\tag{14}
$$

while similar combinations can be used to isolate the differential tensor shift from the σ^- data as well as the tensor shift coefficient of the $^1S_0$ state. From the σ splitting data we find $\Delta\kappa^T = 0.03(8)$ Hz/U_0 and $|\kappa_e^T|=0.02(4)$ Hz/U_0. The data for these measurements is shown in Fig. 8. Similarly, we extracted the tensor shift coefficient from π spectra, exploiting the m_F-dependent term in Eq. 12, yielding $\Delta\kappa^T = 0.02(7)$ Hz/U_0. The measurements here are consistent with zero and were not found to depend on the trapping depth used for a range of 0.85–1.7 U_0, and hence are interpreted as conservative upper limits to the shift coefficients. The error bars represent the standard deviation of many measurements, with the scatter in the data due mainly to laser frequency noise and slight under sampling of the peaks. It is worth noting that the tensor shift of the clock transition is expected to be dominated by the $^3P_0$ shift, and therefore, the limit on κ_e^T can be used as an additional estimate for the upper limit on $\Delta\kappa^T$. Improvements on these limits can be made by going to larger trap intensities to enhance sensitivity, as well as by directly stabilizing the clock laser to components of interest for improved averaging.

Table I summarizes the measured sensitivities to magnetic fields and the lattice potential. The Stark shift coefficients for linear polarization at 813.4280(5) nm are given in units of Hz/(U_T/E_R). For completeness, a recent measurement of the second order Zeeman shift using ^{88}Sr has been included [45], as well as the measured shift coefficient $\Delta\gamma$ for the hyperpolarizability [12] and the upper

TABLE I: Measured Field Sensitivities for ^{87}Sr

Sensitivity	Value	Units	Ref.
$\Delta_B^{(1)}/m_F B$	-108.4(4)	Hz/G	This work
$\Delta_B^{(2)}/B^2$	-0.233(5)	Hz/G^2	[45][a]
$\Delta\kappa^T$	6(20) $\times 10^{-4}$	Hz/(U_T/E_R)	This work[b]
$\Delta\kappa^T$	9(23)$\times 10^{-4}$	Hz/(U_T/E_R)	This work[c]
κ_e^T	5(10)$\times 10^{-4}$	Hz/(U_T/E_R)	This work[c]
κ	-3(7)$\times 10^{-3}$	Hz/(U_T/E_R)	[6][d]
$\Delta\gamma$	7(6)$\times 10^{-6}$	Hz/$(U_T/E_R)^2$	[12][d]

[a] Measured for ^{88}Sr
[b] Measured with π spectra
[c] Measured with $\sigma^\pm$ spectra
[d] Measured with degenerate sublevels

limit for the overall linear lattice shift coefficient κ from our recent clock measurement [6]. While we were able to confirm that the vector shift effect is small and consistent with zero in our system, we do not report a limit for the vector shift coefficient $\Delta\kappa^V$ due to uncertainty in the lattice polarization purity and orientation relative to the quantization axis. In future measurements, use of circular trap polarization can enhance the measurement precision of $\Delta\kappa^V$ by at least two orders of magnitude.

Although only upper limits are reported here, the result can be used to estimate accuracy and linewidth limitations for lattice clocks. For example, in the absence of magnetic fields, the tensor shift can cause line broadening of the transition for unpolarized samples. Given the transition amplitudes in Fig. 4, the upper limit for line broadening, derived from the tensor shift coefficients discussed above, is 5 Hz at U_0. The tensor shift also results in a different magic wavelength for different m_F sublevels, which is constrained here to the few picometer level.

V. COMPARISON OF THE δg MEASUREMENT WITH THEORY AND $^3P_0$ LIFETIME ESTIMATE

The precise measurement of δg provides an opportunity to compare various atomic hyperfine interaction theories to the experiment. To calculate the mixing parameters α_0 and β_0 (defined in Eq. 16 of the Appendix), we first try the simplest approach using the standard Breit-Wills (BW) theory [23, 24] to relate the mixing parameters to the measured triplet hyperfine splitting (hfs). The parameters α (0.9996) and β ($-0.0286(3)$) are calculated from recent determinations of the $^3P_1$ [32] and $^1P_1$ [54] lifetimes. The relevant singlet and triplet single-electron hyperfine coefficients are taken from Ref. [55]. From this calculation we find $\alpha_0 = 2.37(1) \times 10^{-4}$, $\beta_0 = -4.12(1) \times 10^{-6}$, and $\gamma_0 = 4.72(1) \times 10^{-6}$, resulting in $\delta g \mu_0 = -109.1(1)$ Hz/G . Using the mixing values in conjunction with Eq. 4 we find that the $^3P_0$ lifetime is 152(2) s. The agreement with the measured g-factor is excellent, however the BW-theory is known to have problems predicting the $^1P_1$ characteristics based on those of

the triplet states. In this case, the BW-theory framework predicts a magnetic dipole A coefficient for the $^1P_1$ state of -32.7(2) MHz, whereas the experimental value is -3.4(4) MHz [55]. Since δg is determined mainly by the properties of the $^3P_1$ state, it is not surprising that the theoretical and experimental values are in good agreement. Conversely, the lifetime of the $^3P_0$ state depends nearly equally on the $^1P_1$ and $^3P_1$ characteristics, so the lifetime prediction deserves further investigation.

A modified BW (MBW) theory [44, 55, 56] was attempted to incorporate the singlet data and eliminate such discrepancies. In this case $^1P_1$, $^3P_1$, and $^3P_2$ hfs are all used in the calculation, and two scaling factors are introduced to account for differences between singlet and triplet radial wavefunctions when determining the HFI mixing coefficients (note that γ_0 is not affected by this modification). This method has been shown to be successful in the case of heavier systems such as neutral Hg [44]. We find $\alpha_0 = 2.56(1) \times 10^{-4}$ and $\beta_0 = -5.5(1) \times 10^{-6}$, resulting in $\delta g \mu_0 = -117.9(5)$ Hz/G and $\tau^{^3P_0} = 110(1)$ s. Here, the agreement with experiment is fair, but the uncertainties in experimental parameters used for the theory are too small to explain the discrepancy.

Alternatively, we note that in Eq. 6, δg depends strongly on $\alpha_0\alpha$ and only weakly ($< 1\%$) on $\beta_0\beta$, such that our measurement can be used to tightly constrain $\alpha_0 = 2.35(1) \times 10^{-4}$, and then use only the triplet hfs data to calculate β_0 in the MBW theory framework. In this way we find $\beta_0 = -3.2(1) \times 10^{-6}$, yielding $\tau^{^3P_0} = 182(5)$s. The resulting $^1P_1$ hfs A coefficient is $-15.9(5)$ MHz, which is an improvement compared to the standard BW calculation. The inability of the BW and MBW theory to simultaneously predict the singlet and triplet properties seems to suggest that the theory is inadequate for ^{87}Sr. A second possibility is a measurement error of some of the hfs coefficients, or the ground state g-factor. The triplet hfs is well resolved and has been confirmed with high accuracy in a number of measurements. An error in the ground state g-factor measurement at the 10% level is unlikely, but it can be tested in future measurements

TABLE II: Theoretical estimates of δg and $\tau^{^3P_0}$ for ^{87}Sr

	Values used in Calculation $\alpha = 0.9996$ $\beta = -0.0286(3)$				
Calc.	α_0 $\times 10^4$	β_0 $\times 10^6$	$\tau^{^3P_0}$ (s)	$\delta g\mu_0$ m_F(Hz/G)	A^1P_1 (MHz)
BW	2.37(1)	-4.12(1)	152(2)	-109.1(1)	-32.7(2)
MBW I	2.56(1)	-5.5(1)	110(1)	-117.9(5)	-3.4(4)[a]
MBW II	2.35(1)	-3.2(1)	182(5)	-108.4(4)[b]	-15.9(5)
Ref [40]	—	—	132	—	—
Ref [41, 59]	2.9(3)	-4.7(7)	110(30)	-130(15) [c]	—
Ref [8, 9]	—	—	159	106[d]	—

[a] Experimental value [55]
[b] Experimental value from this work
[c] Calculated using Eq. 6
[d] Sign inferred from Figure 1 in Ref. [8]

by calibrating the field in an independent way so that both g_I and δg can be measured. On the other hand, the $^1P_1$ hfs measurement has only been performed once using level crossing techniques, and is complicated by the fact that the structure is not resolved, and that the ^{88}Sr transition dominates the spectrum for naturally abundant samples. Present ^{87}Sr cooling experiments could be used to provide an improved measurement of the $^1P_1$ data to check whether this is the origin of the discrepancy.

Although one can presumably predict the lifetime with a few percent accuracy (based on uncertainties in the experimental data), the large model-dependent spread in values introduces significant additional uncertainty. Based on the calculations above (and many other similar ones) and our experimental data, the predicted lifetime is 145(40) s. A direct measurement of the natural lifetime would be ideal, as has been done in similar studies with trapped ion systems such as In$^+$ [39] and Al$^+$ [57] or neutral atoms where the lifetime is shorter, but for Sr this type of experiment is difficult due to trap lifetime limitations, and the measurement accuracy would be limited by blackbody quenching of the $^3P_0$ state [58].

Table II summarizes the calculations of δg and $\tau^{^3P_0}$ discussed here including the HFI mixing parameters α_0 and β_0. Other recent calculations based on the BW theory [8, 9], ab initio relativistic many body calculations [40], and an effective core calculation [41] are given for comparison, with error bars shown when available.

VI. IMPLICATIONS FOR THE ^{87}SR LATTICE CLOCK

In the previous sections, the magnitude of relevant magnetic and Stark shifts has been discussed. Briefly, we will discuss straightforward methods to reduce or eliminate the effects of the field sensitivities. To eliminate linear Zeeman and vector light shifts the obvious path is to use resolved sublevels and average out the effects by alternating between measurements of levels with the same $|m_F|$. Figure 9 shows an example of a spin-polarized measurement using the $m_F = \pm 9/2$ states for cancelation of the Zeeman and vector shifts. To polarize the sample, we optically pump the atoms using a weak beam resonant with the $^1S_0$-$^3P_1$ ($F = 7/2$) transition. The beam is co-aligned with the lattice and clock laser and linearly polarized along the lattice polarization axis ($\theta = 0$), resulting in optical pumping to the stretched ($m_F = 9/2$) states. Spectroscopy with (blue) and without (red) the polarizing step shows the efficiency of the optical pumping as the population in the stretched states is dramatically increased while excitations from other sublevels are not visible. Alternate schemes have been demonstrated elsewhere [8, 26] where the population is pumped into a single $m_F = \pm 9/2$ state using the $^1S_0$-$^3P_1$ ($F = 9/2$) transition. In our system, we have found the method shown here to be more efficient in terms of atom number in the final state and state purity. The highly efficient
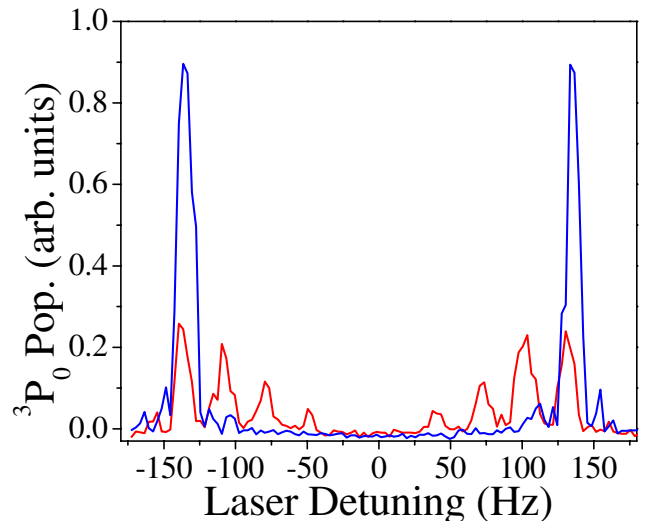

FIG. 9: (color online) The effect of optical pumping via the $^3P_1$ ($F = 7/2$) state is shown via direct spectroscopy with $\theta = 0$. The red data shows the spectrum without the polarizing light for a field of 0.27 G. With the polarizing step added to the spectroscopy sequence the blue spectum is observed. Even with the loss of $\sim 15\%$ of the total atom number due to the polarizing laser, the signal size of the $m_F = \pm 9/2$ states is increased by more than a factor of 4.

optical pumping and high spectral resolution should allow clock operation with a bias field of less than 300 mG for a 10 Hz feature while keeping line pulling effects due to the presence of the other sublevels below 10^{-17}. The corresponding second order Zeeman shift for such a field is only $\sim$21 mHz, and hence knowledge of the magnetic field at the 10% level is sufficient to control the effect below 10^{-17}. With the high accuracy δg-measurement reported here, real time magnetic field calibration at the level of a few percent is trivial. For spin-polarized samples, a new magic wavelength can be determined for the m_F-pair, and the effect of the tensor shift will only be to modify the cancelation wavelength by at most a few picometers if a different set of sublevels are employed. With spin-polarized samples, the sensitivity to both magnetic and optical fields (including hyperpolarizability effects) should not prevent the clock accuracy from reaching below 10^{-17}.

Initial concerns that nuclear spin effects would limit the obtainable accuracy of a lattice clock have prompted a number of recent proposals to use bosonic isotopes in combination with external field induced state mixing [17, 18, 20, 21, 22] to replace the mixing provided naturally by the nuclear spin. In these schemes, however, the simplicity of a hyperfine-free system comes at the cost of additional accuracy concerns as the mixing fields also shift the clock states. The magnitudes of the shifts depend on the species, mixing mechanism, and achievable spectral resolution in a given system. As an example, we discuss the magnetic field induced mixing scheme [20] which was the first to be experimentally demonstrated

for Yb [19] and Sr [45]. For a 10 Hz ^{88}Sr resonance (i.e. the linewidth used in this work), the required magnetic and optical fields (set to minimize the total frequency shift) result in a second order Zeeman shift of -30 Hz and an ac Stark shift from the probe laser of -36 Hz. For the same transition width, using spin-polarized ^{87}Sr, the second order Zeeman shift is less than -20 mHz for the situation in Fig. 9, and the ac Stark shift is less than 1 mHz. Although the nuclear-spin-induced case requires a short spin-polarizing stage and averaging between two sublevels, this is preferable to the bosonic isotope, where the mixing fields must be calibrated and monitored at the 10^{-5} level to reach below 10^{-17}. Other practical concerns may make the external mixing schemes favorable, if for example isotopes with nuclear spin are not readily available for the species of interest. In a lattice clock with atom-shot noise limited performance, the stability could be improved, at the cost of accuracy, by switching to a bosonic isotope with larger natural abundance.

In conclusion we have presented a detailed experimental and theoretical study of the nuclear spin effects in optical lattice clocks. A perturbative approach for describing the state mixing and magnetic sensitivity of the clock states was given for a general alkaline-earth(-like) system, with ^{87}Sr used as an example. Relevant Stark shifts from the optical lattice were also discussed. We described in detail our sign-sensitive measurement of the differential g-factor of the $^1S_0$-$^3P_0$ clock transition in ^{87}Sr, yielding $\mu_0 \delta g = -108.4(4) m_F$ Hz/G, as well as upper limit for the differential and exited state tensor shift coefficients $\Delta \kappa^T = 0.02$ Hz/(U_T/E_R) and $\kappa_e^T = 0.01$ Hz/(U_T/E_R). We have demonstrated a polarizing scheme which should allow control of the nuclear spin related effects in the ^{87}Sr lattice clock to well below 10^{-17}.

[1] S. A. Diddams *et al.*, Science **306**, 1318 (2004).
[2] M. Takamoto *et al.*, Nature **435**, 321 (2005).
[3] M. M. Boyd *et al.*, Science **314**, 1430 (2006).
[4] C. W. Hoyt *et al.*, in *Proceedings of the 20th European Frequency and Time Forum*, Braunschweig, Germany, March 27-30, p. 324-328 (2006).
[5] A. D. Ludlow *et al.*, Phys. Rev. Lett. **96**, 033003 (2006).
[6] M. M. Boyd *et al.*, Phys. Rev. Lett. **98**, 083002 (2007).
[7] R. Le Targat *et al.*, Phys. Rev. Lett. **97**, 130801 (2006).
[8] M. Takamoto *et al.*, J. Phys. Soc. Japan **75**, 10 (2006).
[9] H. Katori *et al.*, Phys. Rev. Lett. **91**, 173005 (2003).
[10] V. Ovsiannikov *et al.*, Quantum Electron. **36**, 3 (2006).
[11] S. G. Porsev *et al.*, Phys. Rev. A **69**, 021403(R) (2004).
[12] A. Brusch *et al.*, Phys. Rev. Lett. **96**, 103003 (2006).
[13] W. H. Oskay *et al.*, Phys. Rev. Lett. **97**, 020801 (2006).
[14] L. Childress *et al.*, Science **314**, 281 (2006).
[15] D. Hayes, P. S. Julienne, and I. H. Deutsch, Phys. Rev. Lett. **98**, 070501 (2007)
[16] I. Reichenbach and I. Deutsch, quant-ph/0702120.
[17] R. Santra *et al.*, Phys. Rev. Lett. **94**, 173002 (2005).
[18] T. Hong *et al.*, Phys. Rev. Lett. **94**, 050801 (2005).
[19] Z. W. Barber *et al.*, Phys. Rev. Lett. **96**, 083002 (2006).
[20] A. V. Taichenachev *et al.*, Phys. Rev. Lett. **96**, 083001 (2006).
[21] T. Zanon-Willette *et al.*, Phys. Rev. Lett. **97**, 233001 (2006).
[22] V. D. Ovsiannikov *et al.*, Phys. Rev. A **75**, 020501 (2007).
[23] G. Breit and L. A. Wills, Phys. Rev. **44**, 470 (1933).
[24] A. Lurio, M. Mandel, and R. Novick, Phys. Rev. **126**, 1758 (1962).
[25] K. R. Vogel *et al.*, IEEE Trans. on Inst. and Meas. **48**, 618 (1999).
[26] T. Mukaiyama *et al.*, Phys. Rev. Lett. **90**, 113002 (2003).
[27] T. H. Loftus *et al.*, Phys. Rev. Lett. **93**, 073003 (2004).
[28] T. H. Loftus *et al.*, Phys. Rev. A **70**, 063413 (2004).
[29] N. Poli *et al.*, Phys. Rev. A **71**, 061403 (2005).
[30] E. A. Curtis, C. W. Oates, and L. Hollberg, Phys. Rev. A **64**, 031403 (2001).
[31] T. Binnewies *et al.*, Phys. Rev. Lett. **87**, 123002 (2001)
[32] T. Zelevinsky *et al.*, Phys. Rev. Lett. **96**, 203201 (2006).
[33] S. Tojo *et al.*, Phys. Rev. Lett. **96**, 153201 (2006).
[34] R. Ciuryło *et al.*, Phys. Rev. A **70**, 062710 (2004).
[35] C. Degenhardt *et al.*, Phys. Rev. A **72**, 062111 (2005).
[36] G. Wilpers *et al.*, Appl. Phys. B **85**, 31 (2006).
[37] T. Ido *et al.*, Phys. Rev. Lett. **94**, 153001 (2005).
[38] M. V. Romalis *et al.*, Phys. Rev. Lett. **86**, 2505 (2001).
[39] T. Becker *et al.*, Phys. Rev. A **63**, 051802 (2001).
[40] S. G. Porsev and A. Derevianko, Phys. Rev. A **69**, 042506 (2004).
[41] R. Santra *et al.*, Phys. Rev. A **69**, 042510 (2004).
[42] L. Olschewski, Z. Phys. **249**, 205 (1972).
[43] H. Kopfermann, *Nuclear Moments*, New York, (1963).
[44] B. Lahaye and J. Margerie, J. Physique **36**, 943 (1975).
[45] X. Baillard *et al.*, physics/0703148.
[46] S. Bize *et al.*, J. Phys. B **38**, S449 (2005).
[47] T. P. Heavner *et al.*, Metrologia **42**, 411 (2005).
[48] H. S. Margolis *et al.*, Science **306**, 1355 (2004).
[49] P. Dubé *et al.*, Phys. Rev. Lett. **95**, 033001 (2005).
[50] T. Schneider *et al.*, Phys. Rev. Lett. **94**, 230801 (2005).
[51] P. J. Blythe *et al.*, Phys. Rev. A **67**, 020501 (2003).
[52] M. V. Romalis and E. N. Fortson, Phys. Rev. A **59**, 4547 (1999).
[53] A. D. Ludlow *et al.*, Opt. Lett. **32**, 641 (2007).
[54] P. Mickelson *et al.*, Phys. Rev. Lett. **95**, 223002 (2005).
[55] H. J. Kluge and H. Sauter, Z. Physik **270**, 295 (1974).
[56] A. Lurio, Phys. Rev. **142**, 46 (1966).
[57] T. Rosenband *et al.*, Phys. Rev. Lett. **98**, 220801 (2007).
[58] X. Xu *et al.*, J. Opt. Soc. Am. B **20**, 5 (2003).
[59] Unpublished HFI coefficients extracted from Ref. [41], R. Santra *private communication.*
[60] S. G. Porsev and A. Derevianko, Phys. Rev. A **74**, 020502 (2006).
[61] G. Breit and I. I. Rabi, Phys. Rev. **38**, 2082 (1932).
[62] S. M. Heider and G. O. Brink, Phys. Rev. A. **16**, 1371 (1977).
[63] G. zu Putlitz, Z. Phys. **175**, 543 (1963).

VII. APPENDIX

The appendix is organized as follows, in the first section we briefly describe calculation of the mixing coefficients needed to estimate the effects discussed in the main text. We also include relevant Zeeman matrix elements. In the second section we describe a perturbative treatment of the magnetic field on the hyperfine-mixed $^3P_0$ state, resulting in a Breit-Rabi like formula for the clock transition. In the final section we solve the more general case and treat the magnetic field and hyperfine interaction simultaneously, which is necessary to calculate the sensitivity of the $^1P_1$, $^3P_1$ and $^3P_2$ states.

A. State mixing coefficients and Zeeman elements

The intermediate coupling coefficients α and β are typically calculated from measured lifetimes and transition frequencies of the $^1P_1$ and $^3P_1$ states and a normalization constraint, resulting in

$$\frac{\alpha^2}{\beta^2} = \frac{\tau^{3P_1}}{\tau^{1P_1}} \left(\frac{\nu_{3P_1}}{\nu_{1P_1}} \right)^3, \; \alpha^2 + \beta^2 = 1. \qquad (15)$$

The HFI mixing coefficients α_0, β_0, and γ_0 are due to the interaction between the pure $^3P_0$ state and the spin-orbit mixed states in Eq. 1 having the same total angular momentum F. They are defined as

$$\begin{aligned}
\alpha_0 &= \frac{\langle ^3P_1, F = I | H_A |^3P_0^0, F = I \rangle}{\nu_{3P_0} - \nu_{3P_1}} \\
\beta_0 &= \frac{\langle ^1P_1, F = I | H_A |^3P_0^0, F = I \rangle}{\nu_{3P_0} - \nu_{1P_1}} \\
\gamma_0 &= \frac{\langle ^3P_2, F = I | H_Q |^3P_0^0, F = I \rangle}{\nu_{3P_0} - \nu_{3P_2}}.
\end{aligned} \qquad (16)$$

Where H_A and H_Q are the magnetic dipole and electric quadrupole contributions of the hyperfine Hamiltonian. A standard technique for calculating the matrix elements is to relate unknown radial contributions of the wavefunctions to the measured hyperfine magnetic dipole (A) and electric quadrupole (Q) coefficients. Calculation of the matrix elements using BW theory [23, 24, 39, 44, 55] can be performed using the measured hyperfine splitting of the triplet state along with matrix elements provided in [24]. Inclusion of the $^1P_1$ data (and an accurate prediction of β_0) requires a modified BW theory [44, 55, 56] where the relation between the measured hyperfine splitting and the radial components is more complex but manageable if the splitting data for all of the states in the $nsnp$ manifold are available. A thorough discussion of the two theories is provided in Refs. [44, 55].

Zeeman matrix elements for singlet and triplet states in the $nsnp$ configuration have been calculated in Ref. [24]. Table III summarizes those elements relevant to the work here, where the results have been simplified by using the electronic quantum numbers for the alkaline-earth case,

but leaving the nuclear spin quantum number general for simple application to different species. Note that the results include the application of our sign convention in Eq. 5 which differs from that in Ref. [24].

B. Magnetic field as a perturbation

To determine the magnetic sensitivity of the $^3P_0$ state due to the hyperfine interaction with the $^3P_1$ and $^1P_1$ states, we first use a perturbative approach to add the Zeeman interaction as a correction to the $|^3P_0\rangle$ state in Eq. 3. The resulting matrix elements depend on spin-orbit and hyperfine mixing coefficients α, β, α_0, β_0, and γ_0. For the $^3P_0$ state, diagonal elements to first order in α_0 and β_0 are relevant, while for $^1P_1$ and $^3P_1$, the contribution of the hyperfine mixing to the diagonal elements can be ignored. All off-diagonal terms of order β^2, $\alpha_0\alpha$, $\alpha_0\beta$, α_0^2, and smaller can be neglected. Due to the selection rules for pure (LS) states, the only contributions of the $^3P_2$ hyperfine mixing are of order $\alpha_0\gamma_0$, γ_0^2, and $\beta_0\gamma_0$. Thus the state can be ignored and the Zeeman interaction matrix M_z between atomic P states can be described in the $\{|^1P_1, F, m_F\rangle, |^3P_0, F, m_F\rangle, |^3P_1, F, m_F\rangle\}$ basis as

$$M_z = \begin{pmatrix} \nu_{1P_1} & M_{1P_1}^{3P_0} & 0 \\ M_{3P_0}^{1P_1} & \nu_{3P_0} & M_{3P_0}^{3P_1} \\ 0 & M_{3P_1}^{3P_0} & \nu_{3P_1} \end{pmatrix}, \qquad (17)$$

where we define diagonal elements as

$$\begin{aligned}
\nu_{3P_0} =& \nu_{3P_0}^0 + \langle ^3P_0^0 | H_Z |^3P_0^0 \rangle \\
& + 2(\alpha\alpha_0 - \beta\beta_0)\langle ^3P_1^0, F = I | H_Z |^3P_0^0 \rangle \\
\nu_{3P_1} =& \nu_{3P_1}^0 + \sum_{F'} \left(\alpha^2 \langle ^3P_1^0, F' | H_Z |^3P_1^0, F' \rangle \right. \\
& \left. + \beta^2 \langle ^1P_1^0, F' | H_Z |^1P_1^0, F' \rangle \right) \\
\nu_{1P_1} =& \nu_{1P_1}^0 + \sum_{F'} \left(\alpha^2 \langle ^1P_1^0, F' | H_Z |^1P_1^0, F' \rangle \right. \\
& \left. + \beta^2 \langle ^3P_1^0, F' | H_Z |^3P_1^0, F' \rangle \right).
\end{aligned} \qquad (18)$$

Off diagonal elements are given by

$$\begin{aligned}
M_{3P_0}^{3P_1} = M_{3P_1}^{3P_0} =& \alpha \sqrt{\sum_{F'} |\langle ^3P_1^0, F' | H_Z |^3P_0^0, F \rangle|^2} \\
M_{3P_0}^{1P_1} = M_{1P_1}^{3P_0} =& \beta \sqrt{\sum_{F'} |\langle ^3P_0^0, F | H_Z |^3P_0^0, F' \rangle|^2}.
\end{aligned} \qquad (19)$$

TABLE III: Zeeman Matrix Elements for Pure $(^{2S+1}L_J^0)$ States

Relevant Elements for the $^3P_0$ State:
$\langle^3P_0^0, F=I\vert H_Z\vert^3P_0^0, F=I\rangle = -g_I m_F \mu_0 B$
$\langle^3P_0^0, F=I\vert H_Z\vert^3P_1^0, F'=I\rangle = (g_s - g_l) m_F \mu_0 B \sqrt{\frac{2}{3I(I+1)}}$
$\langle^3P_0^0, F=I\vert H_Z\vert^3P_1^0, F'=I+1\rangle = (g_s - g_l) \mu_0 B \sqrt{\frac{((I+1)^2 - m_F^2)(4I+6)}{3(I+1)(4(I^2+1)-1)}}$
$\langle^3P_0^0, F=I\vert H_Z\vert^3P_1^0, F'=I-1\rangle = (g_s - g_l) \mu_0 B \sqrt{\frac{(I^2 - m_F^2)(4I-2)}{3I(4I^2-1)}}$
Relevant Diagonal Elements within $^3P_1$ Manifold:
$\langle^3P_1^0, F=I\vert H_Z\vert^3P_1^0, F=I\rangle = \left(\frac{g_l + g_s - g_I(2I(I+1)-2)}{2I(I+1)}\right) m_F \mu_0 B$
$\langle^3P_1^0, F=I+1\vert H_Z\vert^3P_1^0, F=I+1\rangle = \left(\frac{g_l + g_s - 2g_I I}{2(I+1)}\right) m_F \mu_0 B$
$\langle^3P_1^0, F=I-1\vert H_Z\vert^3P_1^0, F=I-1\rangle = \left(-\frac{g_l + g_s + 2g_I(I+1)}{2I}\right) m_F \mu_0 B$
Relevant Diagonal Elements within $^1P_1$ Manifold:
$\langle^1P_1^0, F=I\vert H_Z\vert^1P_1^0, F=I\rangle = \left(\frac{g_l - g_I(I(I+1)-1)}{I(I+1)}\right) m_F \mu_0 B$
$\langle^1P_1^0, F=I+1\vert H_Z\vert^1P_1^0, F=I+1\rangle = \left(\frac{g_l - g_I I}{(I+1)}\right) m_F \mu_0 B$
$\langle^1P_1^0, F=I-1\vert H_Z\vert^1P_1^0, F=I-1\rangle = \left(-\frac{g_l + g_I(I+1)}{I}\right) m_F \mu_0 B$

The eigenvalues of Eq. 17 can be written analytically as three distinct cubic roots

$$
\nu_{m_F}^{\pm} = \frac{\nu_0}{3} \mp \sqrt{\nu_0^2 + 3\nu_1^2} \times
$$
$$
\cos\left[\frac{1}{3}\arccos\left[\mp\frac{2\nu_0^3 + 9\nu_0\nu_1^2 + 27\nu_2^3}{2(\nu_0^2 + 3\nu_1^2)^{3/2}}\right] \pm \frac{2\pi}{3}\right]
$$
$$
\nu_{m_F} \equiv \nu_{^3P_0, m_F} = \frac{\nu_0}{3} + \sqrt{\nu_0^2 + 3\nu_1^2} \times
$$
$$
\cos\left[\frac{1}{3}\arccos\left[\frac{2\nu_0^3 + 9\nu_0\nu_1^2 + 27\nu_2^3}{2(\nu_0^2 + 3\nu_1^2)^{3/2}}\right] + \frac{2\pi}{3}\right], \tag{20}
$$

where we have

$$
\nu_0 = \nu_{^3P_0} + \nu_{^3P_1} + \nu_{^1P_1}
$$
$$
\nu_1 = \left[-\nu_{^3P_0}\nu_{^3P_1} - \nu_{^3P_1}\nu_{^1P_1} - \nu_{^3P_0}\nu_{^1P_1} + (M_{^3P_0}^{^3P_1})^2 \right.
$$
$$
\left. + (M_{^3P_0}^{^1P_1})^2\right]^{\frac{1}{2}} \tag{21}
$$
$$
\nu_2 = \left[\nu_{^3P_0}\nu_{^3P_1}\nu_{^1P_1} - \nu_{^3P_1}(M_{^3P_0}^{^1P_1})^2 - \nu_{^1P_1}(M_{^3P_0}^{^3P_1})^2\right]^{\frac{1}{3}}.
$$

Since the main goal is a description of the $^3P_0$ state sensitivity, the solution can be simplified when one considers the relative energy spacing of the three states, and that elements having terms β, $\alpha\beta$, and smaller are negligible compared to those proportional to only α. Therefore we can ignore $M_{^3P_0}^{^1P_1}$ terms and find simplified eigenvalues arising only from the interaction between $^3P_1$ and $^3P_0$ that can be expressed as a Breit-Rabi like expression for the $^3P_0$ state given by

$$
\nu_{^3P_0, m_F} = \frac{1}{2}\left(\nu_{^3P_0} + \nu_{^3P_1}\right) + \frac{1}{2}\left(\nu_{^3P_0} - \nu_{^3P_1}\right)
$$
$$
\times \sqrt{1 + 4\frac{\sum_{F'}\alpha^2\vert\langle^3P_0^0, F\vert H_Z\vert^3P_1^0, F'\rangle\vert^2}{(\nu_{^3P_0} - \nu_{^3P_1})^2}}. \tag{22}
$$

For magnetic fields where the Zeeman effect is small compared to the fine-structure splitting, the result is identical to that from Eq. 8 of the main text. The magnetic
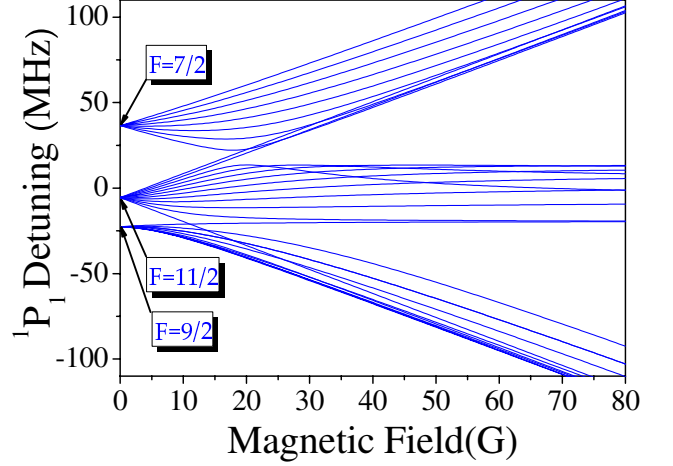

FIG. 10: (color online) Magnetic sensitivity of the $^1P_1$ state calculated with the expression in Eq. 24 using $A = -3.4$ MHz and $Q = 39$ MHz [55]. Note the inverted level structure.

sensitivity of the clock transition (plotted in Fig. 2) is determined by simply subtracting the $\langle^3P_0^0\vert H_Z\vert^3P_0^0\rangle$ term which is common to both states.

C. Full treatment of the HFI and magnetic field

For a more complete treatment of the Zeeman effect we can relax the constraint of small fields and treat the hyperfine and Zeeman interactions simultaneously using the spin-orbit mixed states in Eq. 1 as a basis. The total Hamiltonian is written $H_{\text{total}} = H_Z + H_A + H_Q$ including hyperfine H_A and quadrupole H_Q effects in addition to the Zeeman interaction H_Z defined in Eq. 5 of the main
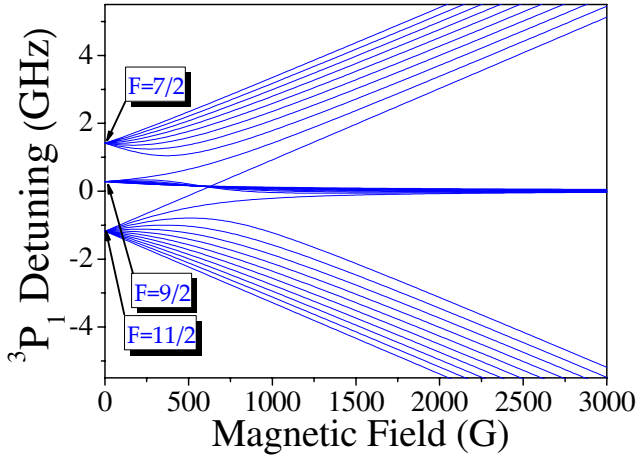
FIG. 11: (color online) Magnetic sensitivity of the $^3P_1$ state calculated with the expression in Eq. 24 using $A = -260$ MHz and $Q = -35$ MHz [63].

Diagonalization of the full space using Eq. 23 does not change the $^3P_0$ result discussed above, even for fields as large as 10^4 G. This is not surprising since the $^3P_0$ state has only one F level, and is therefore only affected by the hyperfine interaction through state mixing which was already accounted for in the previous calculation. Alternatively, for an accurate description of the $^1P_1$, $^3P_1$ and $^3P_2$ states, Eq. 23 must be used. For an alkaline-earth $^{2S+1}L_1$ state in the $|I, J, F, m_F\rangle$ basis we find an analytical expression for the field dependence of the $F = I, I \pm 1$ states and sublevels. The solution is identical to Eq. 20 except we replace the frequencies in Eq. 21 with those in Eq. 24. We define the relative strengths of magnetic, hyperfine, and quadrupole interactions with respect to an effective hyperfine-quadrupole coupling constant $W_{AQ} = A + \frac{3Q}{4I(1-2I)}$ as $X_{BR} = \frac{\mu_0 B}{W_{AQ}}$, $X_A = \frac{A}{W_{AQ}}$, and $X_Q = \frac{Q}{I(1-2I)W_{AQ}}$, respectively. The solution is a generalization of the Breit-Rabi formula [61] for the $^{2S+1}L_1$ state in the two electron system with nuclear spin I. The frequencies are expanded in powers of X_{BR} as

text. The Hamiltonian H_{total} can be written as

$$H_{\text{total}} = H_Z + A\vec{I}\cdot\vec{J}$$
$$+ Q\frac{\frac{3}{2}\vec{I}\cdot\vec{J}(2\vec{I}\cdot\vec{J}+1) - IJ(I+1)(J+1)}{2IJ(2I-1)(2J-1)}. \quad (23)$$

$$\nu_0 = -2W_{AQ}\left[1 + \frac{3g_I}{2}m_F X_{BR}\right]$$

$$\nu_1 = W_{AQ}\sqrt{X_{\text{eff}}^{\nu_1}}\left[1 + \frac{2(g_{\text{eff}} - g_I)X_A + 3g_{\text{eff}}X_Q}{X_{\text{eff}}^{\nu_1}}m_F X_{BR} + \frac{(g_{\text{eff}}+g_I)^2\left(1 - \frac{3m_F^2 g_I^2}{(g_{\text{eff}}+g_I)^2}\right)}{X_{\text{eff}}^{\nu_1}}X_{BR}^2\right]^{\frac{1}{2}}$$

$$\nu_2 = W_{AQ}\sqrt[3]{I(I+1)X_{\text{eff}}^{\nu_2}}\left[1 + \frac{X_A^2\left(\frac{g_{\text{eff}}}{I(I+1)}+g_I\right) + X_Q^2\frac{3(1-2I)(3+2I)}{16}\left(\frac{g_{\text{eff}}}{I(I+1)}-g_I\right) - X_A X_Q\left(g_{\text{eff}}(2-\frac{3}{2I(I+1)})+g_I\right)}{X_{\text{eff}}^{\nu_2}}m_F X_{BR}\right.$$

$$\left. + \frac{m_F^2 X_A\frac{2g_I g_{\text{eff}}}{I(I+1)} + X_Q\frac{(g_{\text{eff}}+g_I)^2}{2}(1 - \frac{3m_F^2 g_{\text{eff}}^2}{I(I+1)(g_{\text{eff}}+g_I)^2})}{X_{\text{eff}}^{\nu_2}}X_{BR}^2 + \frac{\frac{g_I\left((g_{\text{eff}}+g_I)^2-(g_I m_F)^2\right)}{I(I+1)}}{X_{\text{eff}}^{\nu_2}}m_F X_{BR}^3\right]^{\frac{1}{3}}, \quad (24)$$

with abbreviations

$$X_{\text{eff}}^{\nu_1} = I(I+1)\left(X_A + \frac{X_Q}{4} - I(I+1)X_Q(X_A-1)\right) - 1$$
$$X_{\text{eff}}^{\nu_2} = X_{\text{eff}}\left(X_Q X_{\text{eff}} + \left(X_A^2 - X_Q^2\frac{3(3+2I)(1-2I)}{16}\right)\right)$$
$$X_{\text{eff}} = X_A + X_Q\frac{(3+2I)(1-2I)}{4} \quad (25)$$
$$g_{\text{eff}} = \frac{(g_l+g_s)}{2} + \frac{(g_l-g_s)}{4}(L(L+1)-S(S+1)).$$

The resulting Zeeman splitting of the $5s5p^1P_1$ and $5s5p^3P_1$ hyperfine states in ^{87}Sr is shown in Fig. 10 and Fig. 11. For the more complex structure of $^3P_2$, we have solved Eq. 23 numerically, with the results shown in Fig. 12. The solution for the $^1P_1$ state depends strongly on the quadrupole (Q) term in the Hamiltonian, while for the $^3P_1$ and $^3P_2$ states the magnetic dipole (A) term is dominant.
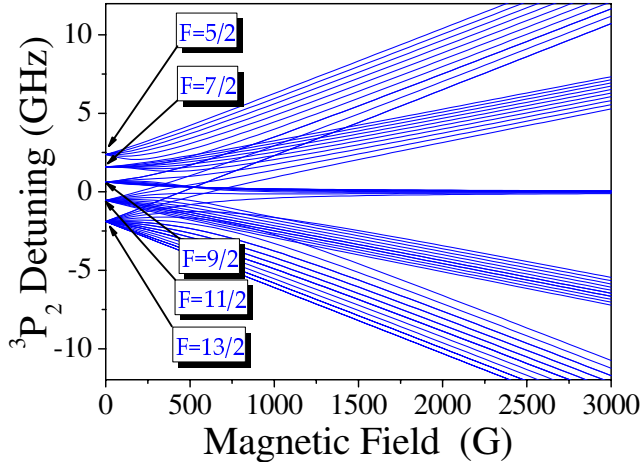
FIG. 12: (color online) Magnetic sensitivity of the $^3P_1$ state calculated numerically with Eq. 23 using A=-212 MHz and Q=67 MHz [62].